

Dopant-Free Hydrogels with Intrinsic Photoluminescence and Biodegradable Properties

Yung-Hao Tsou, Xue-Qing Zhang,* Xin Bai, He Zhu, Zhongyu Li, Yanlan Liu, Jinjun Shi, and Xiaoyang Xu*

Photoluminescent hydrogels that function as both injectable scaffolds and fluorescent imaging probes hold great potential for therapeutics delivery and tissue engineering. Current fluorescent hydrogels are fabricated by either conjugating or doping a fluorescent dye, fluorescent protein, lanthanide chelate, or quantum dot into polymeric hydrogel matrix. Their biomedical applications are severely limited due to drawbacks such as photostability, carcinogenesis, and toxicity associated with the above-mentioned dopants. Here, a successful development of dopant-free photoluminescent hydrogels in situ formed by crosslinking of biocompatible polymer precursors is reported, which can be synthesized by incorporating an amino acid to a citric acid based polyester oligomer followed by functionalization of multivalent crosslinking group through a convenient transesterification reaction using *Candida Antarctica* Lipase B as a catalyst. It is demonstrated that the newly developed hydrogels possess tunable degradation, intrinsic photoluminescence, mechanical properties, and exhibit sustained release of various molecular weight dextrans. In vivo study shows that the hydrogels formed in situ following subcutaneous injection exhibit excellent biocompatibility and emit strong fluorescence under visible light excitation without the need of using any traditional organic dyes. Their in vivo degradation profiles are then depicted by noninvasively monitoring fluorescence intensity of the injected hydrogel implants.

insoluble polymer matrices that can retain large amounts of water.^[1] Due to their unique biocompatibility, compliant elasticity, flexible methods of synthesis, range of constituents, and highly hydrated tissue-like environment for cell and tissue growth, hydrogels have been the material of choice for many biomedical applications.^[2,3] Injectable hydrogels, which can be administered via minimally invasive procedures and appropriately fill irregular-shaped defects by acting as 3D scaffolds, have received much attention due to their widespread applications in the fields of drug delivery, tissue engineering, and regenerative medicine.^[4] Recently, there has been an increasing demand for the development of biodegradable and injectable hydrogels endowed with fluorescent imaging moieties to further enhance the functions of the biomaterials.^[5] For example, hydrogel-based cell transplantation requires accommodating cells in a 3D microenvironment and a noninvasive in vivo imaging capability for investigating donor distribution. Real-time fluorescent imaging can measure degradation rate and

1. Introduction

Hydrogels are 3D polymeric networks formed from hydrophilic homopolymers, copolymers, or macromers crosslinked to form


determine distribution trajectory of the implanted scaffolds in vivo without terminating the host, which helps to prevent inaccurate conclusions derived from broad batch-to-batch and animal-to-animal variations. Such in situ measurements for biomaterials with programmed degradability provide more precise assessment of the in vivo fate of the implanted hydrogels seeded with cells. The photoluminescent hydrogel can be engineered to offer multimodal actions of drug release, cell delivery, and soft tissue engineering with imaging functions.

Conventionally, fluorescent hydrogels are fabricated by either conjugating or doping hydrogel matrix with fluorescent moieties such as organic dye, fluorescent protein, colloidal semiconductor nanocrystal, metal–ligand complex, and lanthanide ions.^[6,7] However, among them, organic dye and fluorescent protein are subjected to certain limitations such as photobleaching and cellular toxicity.^[8] Semiconductor nanocrystals also pose risks to human health and the environment under certain conditions.^[9] Similarly, toxicities from the heavy metal contents of metal–ligand complex and lanthanide ion imaging probes evoke significant safety concerns for their biomedical applications especially for their long-term use in vivo.^[10] Additionally, the aforementioned fluorescent moieties are solely imaging probes, and have to be ancillary to other materials and devices. Such mixed systems are overly

Y.-H. Tsou, H. Zhu, Z. Y. Li, Prof. X. Y. Xu
Department of Chemical and Materials Engineering
New Jersey Institute of Technology
Newark, NJ 07102, USA
E-mail: xiaoyang@njit.edu

X. Bai, Prof. X.-Q. Zhang
Engineering Research Center of Cell & Therapeutic Antibody
Ministry of Education, School of Pharmacy
Shanghai Jiao Tong University
800 Dongchuan Road, Shanghai 200240, P. R. China
E-mail: xueqingzhang@sjtu.edu.cn

Dr. Y. L. Liu, Prof. J. J. Shi
Center for Nanomedicine and Department of Anesthesiology
Brigham and Women's Hospital
Harvard Medical School
Boston, MA 02115, USA

 The ORCID identification number(s) for the author(s) of this article can be found under <https://doi.org/10.1002/adfm.201802607>.

DOI: 10.1002/adfm.201802607

complicated, which inflicts serious challenges to mechanistic investigations on the structure–function relationships and engineering efforts for further optimization of their multifunctional properties. Recently, the attempt at fabrication of an injectable hydrogel by using silk protein sericin has been explored.^[7] The gel was found to exhibit photoluminescence due to the intrinsic autofluorescence of sericin polypeptide. Nevertheless, the low quantum efficiency, untunable fluorescence property, eliciting immune response, and the use of toxic glutaraldehyde as the cross-linker raise concerns for its biomedical applications. Very recently, biodegradable polymers have been reported for the development of implanted elastomers and drug-loaded nanoparticles.^[11] These newly developed biodegradable polymers display superior biocompatibility both in vitro and in vivo, relative high quantum yields, photobleaching resistance, and tunable emission up to near-infrared wavelengths, and thus have potential biomedical applications such as drug delivery nanocarriers and implanted scaffolds. However, the efforts to fabricate a hydrogel using such biodegradable polymers were unsuccessful due to the lack of functional cross-linking molecules on the oligomers.

In this work, we developed a robust dopant-free biodegradable hydrogel platform with intrinsic photoluminescence that provides (1) in vivo postimplantation imaging and tracking function, (2) ability to release diverse payloads in a sustained manner, (3) minimally invasive delivery capability (i.e., direct injection), and (4) tunable physicochemical properties and versatile biofunctionalization capacity. It is noteworthy that these multifunctional hydrogels can be fabricated into implantable drug carriers and cellular scaffolds while also functioning as imaging probes. A library of biodegradable polymers with different photoluminescent properties were synthesized by using biocompatible starting chemicals including citric acid, poly(ethylene glycol)-diol (PEG-diol), and amino acids, and further modified with multi-thiol functional groups through a high-efficient *Candida antarctica* Lipase B (CALB) enzyme-assisted transesterification reaction (Figure S1, Supporting Information). The yielded multivalent thiol-functionalized polymers were then combined with multiarm PEG acrylates or maleimides for in situ formation of biodegradable and biocompatible hydrogels with diverse physicochemical properties through chemical cross-linking (Figure 1). We investigated the impact of the formulations and gelation conditions on the sol-to-gel transition, mechanical and degradation properties of the formed hydrogels. Release profiles of various molecular weight dextrans as model drugs from the hydrogels were also examined. The hydrogels also showed strong and tunable fluorescent emissions from blue to red. In addition, cell-seeded or encapsulated hydrogels showed excellent biocompatibility, indicating their great promise for cell delivery. When subcutaneously injected into nude mice, fluorescence bioimaging of the hydrogels formed in vivo was conducted to demonstrate their potential use in therapeutics delivery, noninvasive tissue imaging, and engineering.

2. Results and Discussions

2.1. Hydrogel Synthesis and Characterization

Citrate acid was reacted with hexaethylene glycol via a facile polycondensation reaction, and serine or cysteine was added

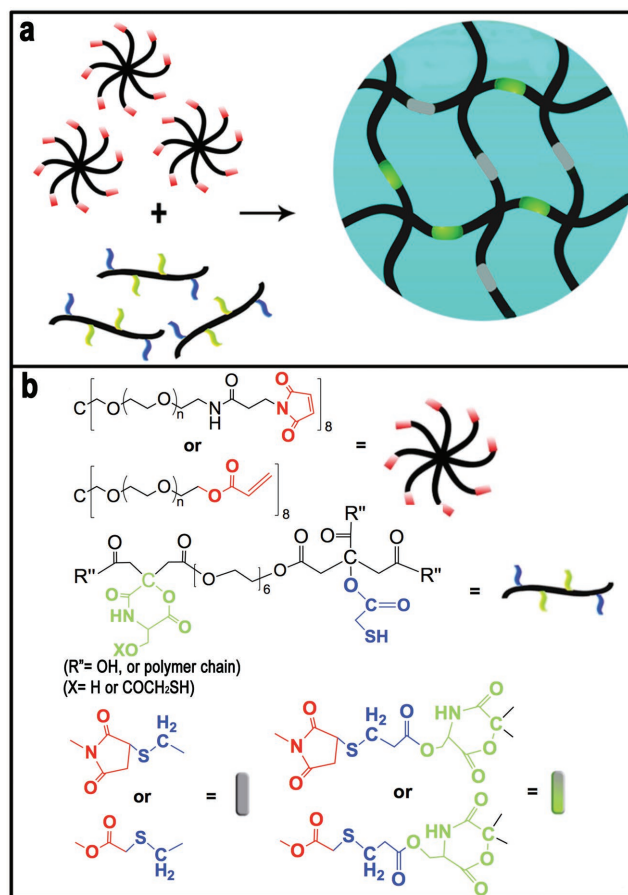


Figure 1. a) A schematic demonstration of hydrogel formation in situ through cross-linking thiolated photoluminescent polyester and multiarm functionalized PEG via maleimide–thiol conjugate addition or an acrylate–thiol Michael addition, and b) chemical structures of the oligomers and cross-linking polymers.

to the reaction of citric acid and hexaethylene glycol to prepare photoluminescent oligomers (CHPO-Ser and CHPO-Cys) (Figure S1, Supporting Information). The incorporation of amino acid resulted in the formation of a six-membered ring chromophore through the amidation reaction between the unreacted carboxylic acid on the citrate and the N-terminus of an amino acid, followed by an esterification reaction between the free carboxylic acid of the amino acid molecule and the hydroxyl group remaining on citrate. The ring contributed strong photoluminescent emitting due to the electrons hyperconjugation over the ring. The polyester oligomers were further reacted with an ethyl ester of a thiol acid using CALB-immobilized on acrylic resin as a catalyst, introducing multivalent thiol functional groups through a transesterification reaction. The synthesis of thiol-functionalized oligomers was shown using CHPO-Ser-ET as a representative oligomer in Figure S1 (Supporting Information). By reacting the photoluminescent CHPO-Ser-ET and CHPO-Cys-ET oligomers with multiarm PEG acrylates or maleimides through chemical cross-linking under physiologically buffered conditions, it was possible to fabricate a library of biodegradable and injectable hydrogels which not only contained tunable self-fluorescent properties,

but also possessed diverse mechanical and physiochemical properties (Figure 1).

Characterizations of thiol-functionalized polymers were conducted using CHPO-Ser-ET as a representative oligomer, except as otherwise specified. The Fourier transform infrared (FTIR) spectra confirmed the presence of $-\text{SH}$ at 2560 cm^{-1} , $-\text{C}(=\text{O})\text{NH}-$ at 1653 cm^{-1} , $-\text{CH}_2-$ at 2887 cm^{-1} , and $-\text{C}=\text{O}$ at 1735 cm^{-1} (Figure S2a, Supporting Information). The average molecular mass of CHPO-Ser-ET measured by matrix-assisted laser desorption/ionization time-of-flight mass spectroscopy (MALDI-TOF-MS) was $\approx 1272\text{ Da}$ (Figure S2b, Supporting Information). The ^1H NMR spectra (500 MHz, CDCl_3 , δ) of CHPO and CHPO-Ser-ET showed the presence of the peaks at 4.29 and 3.66 ppm ($-\text{OCH}_2\text{CH}_2-$ from hexaethylene glycol), 2.88 and 2.95 ppm ($-\text{CH}_2-$ from citric acid), 3.31 and 2.07 ppm from $-\text{CH}_2-$ of $-\text{CH}_2\text{SH}$ and $-\text{SH}$ respectively, which confirmed the incorporation of thiol moieties into the oligomer (Figure S2c,d, Supporting Information). CHPO-Cys-ET exhibited similar ^1H NMR spectra to CHPO-Ser-ET (Figure S2e, Supporting Information). The ^{13}C NMR (500 MHz, CDCl_3 , δ) was obtained to verify the presence of the ring structure on the oligomer chain. For CHPO polyester without the conjugate of serine, the peak at about 43 ppm was assigned to the carbon next to the central carbon of hexaethyleneglycol. Peaks at 64, 68, and 69 ppm were assigned to $-\text{O}-\text{CH}_2\text{CH}_2-$ from hexaethyleneglycol. Peaks at 71 and 73 ppm were assigned to the central carbon of hexaethyleneglycol, and peaks at 170–175 ppm were assigned to carbonyl ($\text{C}=\text{O}$) groups from citric acid (Figure S3a, Supporting Information). In the ^{13}C NMR spectra of CHPO-Ser, there was a clear peak located at 59 ppm indicating the carbon 39 of the ring structure (Figure S3b, Supporting Information). The results demonstrated the presence of a six-membered ring formed on CHPO-Ser oligomer which was responsible for the fluorescence property. In addition, the carbon 40 next to $-\text{SH}$ present in 25.8 ppm confirmed that thiol moieties were incorporated into CHPO-Ser-ET (Figure S3c, Supporting Information). The number of thiol moieties on CHPO-Ser-ET were determined by Ellman's reagent (Thermo Fisher Scientific). The result indicated that there were 5–7 thiol moieties conjugated on each oligomer molecule. The above characterization confirmed successful synthesis of CHPO-Ser-ET.

The yielded oligomers (CHPO-Ser-ET or CHPO-Cys-ET) were then combined with multiarm (four- or eight-arm) functionalized PEG to form photoluminescent hydrogels in a physiological buffer at ambient temperature through a maleimide–thiol conjugate addition or an acrylate–thiol Michael addition (Figure 1a,b). The hydrogels were injectable and moldable as shown in Figure 2a,c, and showed bright photoluminescent properties under 365 and 450 nm excitation wavelength (Figure 2b,d). The formation of hydrogels was confirmed by the vial-tilting method as shown in Figure 2e,f.

2.2. Photoluminescent Characterizations of the Oligomers and Hydrogels

Intrinsic photoluminescence property of biomaterials is a landmark in the future of biomedicine applications. In this study, we found that both the synthesized oligomers, CHPO-Cys-ET

and CHPO-Ser-ET, and their hydrogels formulated with eight-arm PEG-maleimide showed strong emitted fluorescence. The fluorescent excitation and emission spectra of the oligomer solutions were similar to that of their respective PEG hydrogels. Figure 3a,c showed that both CHPO-Cys-ET oligomer and its PEG hydrogel emitted the strongest fluorescence at 450 nm when excited at 360 nm, while the maximum excitation and emission wavelengths for CHPO-Ser-ET oligomer and its hydrogel were 420 and 525 nm, respectively (Figure 3b,d). Compared with CHPO-Cys-ET solution and its hydrogel which were excited at the wavelength range from 320 to 400 nm, the CHPO-Ser-ET solution and hydrogel absorbed a wider range of wavelength (340–500 nm) and emitted tunable fluorescence characteristics under visible light up to 725 nm. Additionally under the same conditions, such as oligomer concentrations and the photomultiplier tube (PMT) gain setting on the microplate reader among many others, the fluorescence intensity of CHPO-Ser-ET from solution to hydrogel decreased $\approx 10.8\%$ (185–165 a.u.) under the maximum excitation wavelength at 420 nm; however, CHPO-Cys-ET/PEG hydrogel decreased $\approx 33.3\%$ (1500–1000 a.u.) in fluorescence intensity under 365 nm excitation compared to the CHPO-Cys-ET solution, indicating that the CHPO-Ser-ET/PEG hydrogel had better penetrating property under visible wavelength. It has also been demonstrated that CHPO-Cys-ET/PEG hydrogel had higher emission intensity than that of CHPO-Ser-ET/PEG hydrogel when excited at a short wavelength light (365 nm), while CHPO-Ser-ET/PEG hydrogel showed superior light emission intensity at longer excitation wavelength (488 nm) as shown in Figure 3e,f. Both CHPO-Ser-ET and CHPO-Cys-ET showed high quantum yield, ≈ 16.42 and $\approx 36.41\%$, respectively (Figure S4, Supporting Information). These results confirmed the feasibility of noninvasive imaging for in vivo tracking and monitoring distribution and degradation of the injected CHPO-Ser-ET/PEG hydrogel implant.

2.3. Degradation, Gelation Time, and Mechanical Properties of the Photoluminescent Hydrogels

Hydrogel degradation can have significant impact on the spatiotemporal release profile of therapeutics, material fate in tissue-engineering formulations, and the overall foreign body response to the implant.^[12] Hydrogel degradation is mainly controlled by the crosslink density established by the functionalized multiarm PEG used, polymer concentration, and crosslink condition.^[3] It is important to investigate the relationship between gel formulations and degradation, as well as the physicochemical and mechanical properties of the prepared hydrogels. To study hydrogel degradation and mechanical properties, CHPO-Ser-ET was used as a representative oligomer to prepare cylinder shape hydrogels with various functionalized PEGs at a fixed polymer concentration of 10 wt% under different buffer conditions (Figure 4a,b). As shown in Figure 4c, hydrogels formed with eight-arm PEG-maleimide demonstrated the most prolonged degradation timeline of up to 25 d than the other test formulations. Increasing the arm number of functionalized PEG delayed hydrogel degradation, confirming the influence of crosslink density. Two different types of degradation profiles were observed: G2 and G8 were gradually degraded

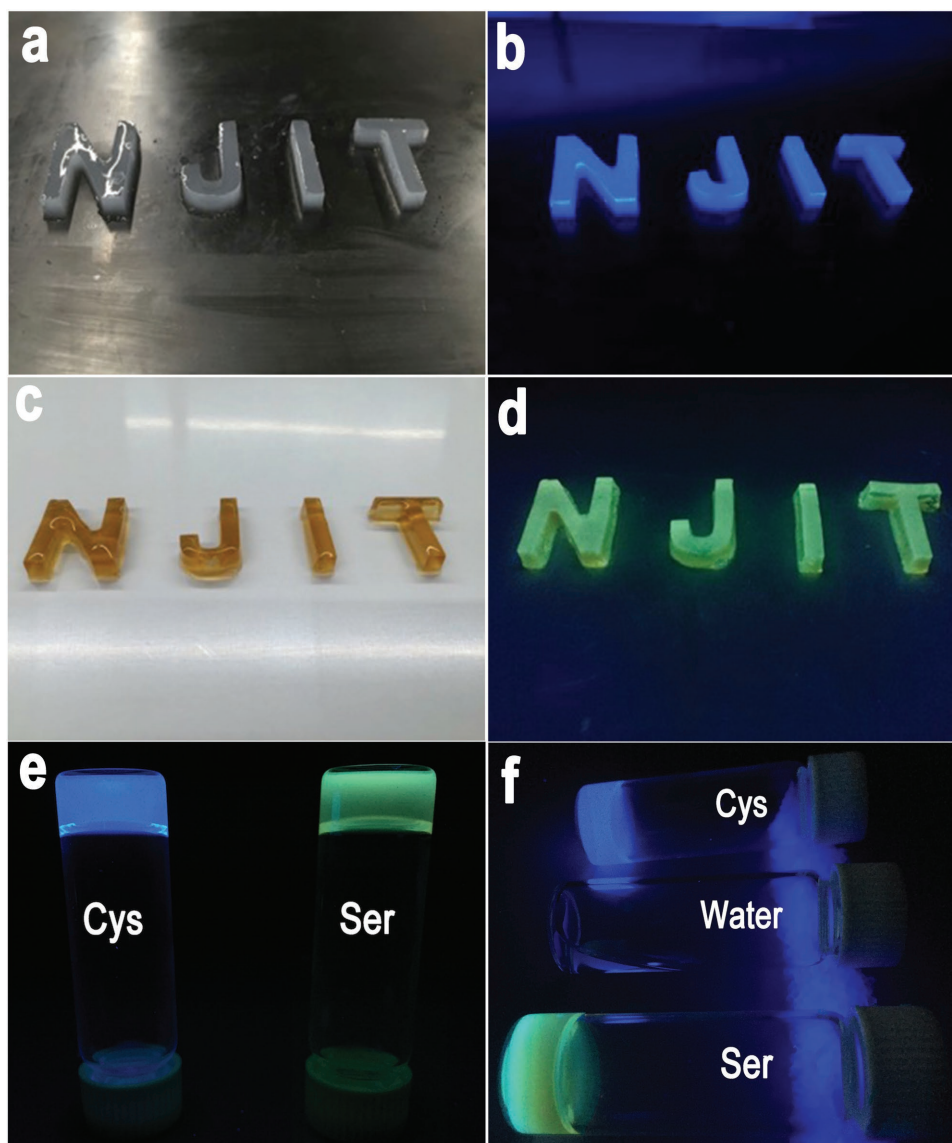


Figure 2. Image of hydrogels formulated with CHPO-Cys/Ser-ET and eight-arm PEG-maleimide a) under visible light and b) under UV light (365 nm) in dark room; image of CHPO-Ser-ET/eight-arm PEG-maleimide hydrogels c) under visible light and d) under UV light (450 nm) in dark; e) image of both CHPO-Cys-ET/PEG hydrogels (blue) and CHPO-Ser-ET/PEG hydrogels (green) in flipped vials under UV light (365 nm) in dark; and f) image of CHPO-Cys-ET/PEG hydrogels (blue), CHPO-Ser-ET/PEG hydrogels (green), and water in tilted vials under UV light (365 nm) in dark. E and F indicate the formation of hydrogels. All hydrogels shown in (a)–(f) were fabricated with polymer concentration of 10 wt% in PBS (pH 7.4) at ambient temperature.

and the others went on quick bulk degradation, indicating that the hydrogels crushed at specific time. For example, G6 only had 40% weight loss at day 6 but it was completely degraded by day 7. This was likely due to the low crosslink density of the formed hydrogel that led to bulk degradation. Specifically, at first the network system with relatively low crosslink density could still hold a stable hydrogel formation. However, during the degradation process a bond between thiol and maleimide/acrylate was broken leading to the breaking of the neighboring bonds and causing the network system to be quickly destroyed. It seemed that ionic strength had little effect on hydrogel degradation when comparing the two hydrogels formed with the same eight-arm PEG-maleimide in different buffers (G2 vs G8). Similarly, there was no significant difference in degradation

profiles of hydrogels prepared in phosphate buffers at pH within the range 7.4–8.0 (G3 vs G5, G4 vs G6). FTIR investigations on the hydrogels formulated with CHPO-Ser-ET and eight-arm PEG-maleimide showed there was no significant C=O IR peak at 1685–1710 cm^{-1} at 36 and 48 h; however, there was clearly C=O peak after 96 h continuous incubation of hydrogel at 37 °C in phosphate buffer, indicating that the hydrogels underwent hydrolysis degradation (Figure 4d).

The sol-to-gel transition and mechanical properties of hydrogels formed through the combination of CHPO-Ser-ET oligomer and eight-arm PEG functionalized with maleimide or acrylate at various polymer concentrations (5–10 wt%) were also studied by dynamic rheology. The time point where storage and loss modulus crossed over (i.e., $\tan(\delta) = G'/G'' = 1$) was

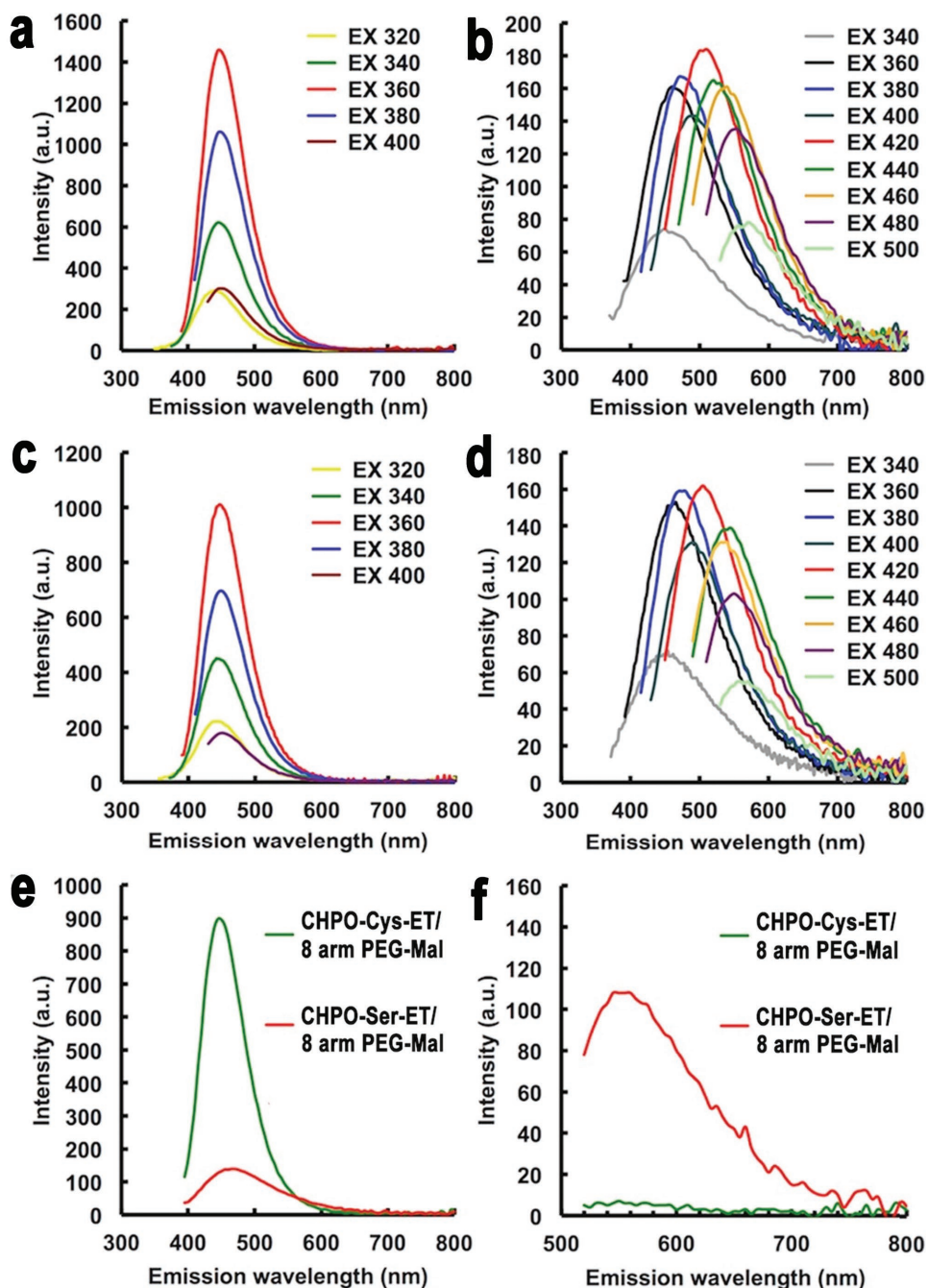


Figure 3. Fluorescent emission spectrum characterization. a,b) Emission spectra of water solution of CHPO-Cys-ET oligomer and CHPO-Ser-ET oligomer; and c,d) emission spectra of CHPO-Cys-ET/eight-arm PEG-maleimide hydrogel and CHPO-Ser-ET/eight-arm PEG-maleimide hydrogel. e) Emission spectra of CHPO-Cys-ET/eight-arm PEG-maleimide and CHPO-Ser-ET/eight-arm PEG-maleimide hydrogels when excited at a fixed wavelength of 360 nm; and f) emission spectra of CHPO-Cys-ET/eight-arm PEG-maleimide and CHPO-Ser-ET/eight-arm PEG-maleimide hydrogels at a fixed excitation wavelength of 488 nm. Each emission spectral curve correlated with certain excitation wavelength from 200 to 800 nm and emission curve was not shown if the intensity is less than 60 a.u.

used to define the onset of gelation. Not surprisingly, hydrogels with higher polymer concentrations demonstrated superior mechanic properties and decreased gelation time compared to hydrogels with lower polymer concentrations (Figure 4e,f). For hydrogels G2, G4, G6, and G8, an increase in the polymer concentration from 5 to 10 wt% resulted in more than tenfold

increase in storage modulus. This was likely a result of the establishment of more crosslinked networks when increasing content of PEG and CHPO-Ser-ET oligomer, thus raising storage modulus (Figure S5a,b, Supporting Information).

Equilibrium swelling ratio (Q_m) of a hydrogel network is an indication of overall crosslinked structure, and a lower swelling

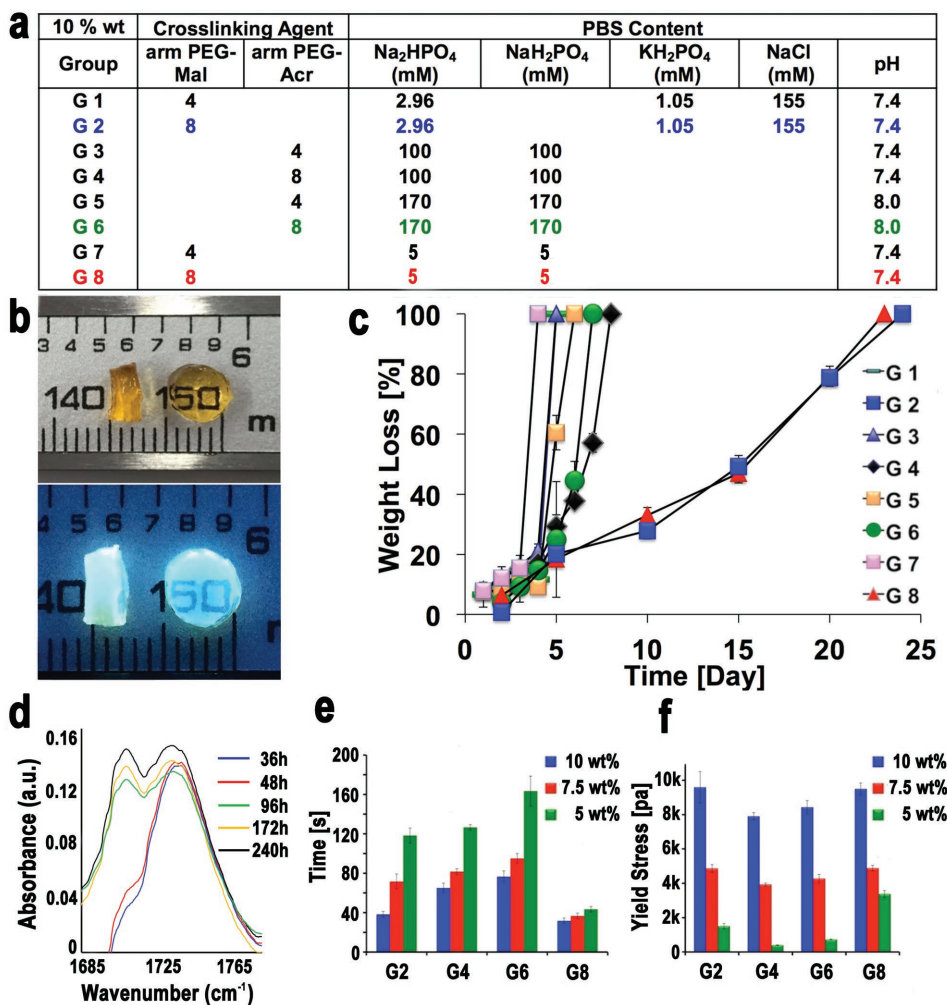


Figure 4. Degradation and dynamic rheology studies of hydrogels fabricated with variant formulations. a) Hydrogels were fabricated with CHPO-Ser-ET and different multifunctional PEGs cross-linkers at a fixed polymer concentration of 10 wt% under different buffer conditions (e.g., varying solution pH or buffer composition and concentrations). b) The image of CHPO-Ser-ET/eight-arm PEG-maleimide hydrogel without excitation (top) and with excitation at 450 nm wavelength (bottom). c) In vitro degradation of the CHPO-Ser-ET/PEG hydrogels in PBS (pH = 7.4) at 37 °C. d) FTIR spectra of CHPO-Ser-ET/eight-arm PEG-maleimide hydrogels incubated for varied periods at 37 °C in PBS indicating the change in the C=O peak (1685–1750 cm⁻¹) as a result of hydrogel degradation. e) Gelation times measured by dynamic rheology for hydrogels formulated with CHPO-Ser-ET and different eight-arm PEGs at varying polymer concentrations at 37 °C (*n* = 5). f) Yield stress of hydrogels formulated with CHPO-Ser-ET and different eight-arm PEGs at varying polymer concentrations (*n* = 5). Data are presented as the mean ± standard deviation (*n* = 5).

ratio indicates a tighter crosslinked network.^[13] The CHPO-Ser-ET/eight-arm PEG hydrogels showed different Q_m values, indicating different crosslink densities of the resultant monomers (Figure S5c, Supporting Information). Hydrogels with a lower Q_m , such as G2 and G8 exhibited a more prolonged degradation timeline, quicker sol-to-gel transition and stronger storage modulus on the order of 1000–10 000 Pa at full gelation, suggesting the influence of crosslink density (Figure 4c and Figure S5a,b, Supporting Information). This low-to-moderate swelling behavior and network characteristics offer great potential benefits in applications of wound healing and tissue regeneration. With the same oligomer compositions, hydrogels formed faster at 37 °C when compared to those formed at 25 °C. This difference was due to the increased reactivity of maleimide–thiol conjugate addition or acrylate–thiol Michael addition at higher temperature (Figure S5d, Supporting Information). Overall,

these data indicated that gelation kinetics, degradation, and mechanical properties of the designed photoluminescent hydrogels could be tailored for a variety of biomedical applications by adjusting polymer concentration, gelation temperature, and PEG species selection along with minor modifications to the solvent buffer conditions (e.g., varying solution pH or ionic strength and concentrations).

2.4. Loading and Release of Macromolecules from Hydrogel Formulations

To demonstrate the utility of the hydrogels for drug delivery, the release kinetics of macromolecules from hydrogel formulations were measured using near-infrared fluorescent dye labeled dextrans (NIR-dextrans) with different molecular weights as model

drugs. NIR-dextran (6 and 100 kDa) were encapsulated within 10 wt% hydrogels formulated with CHPO-Ser-ET oligomer and different eight-arm PEGs (G2, G4, G6, and G8 as described in Figure 4a), and *in vitro* release studies were conducted in phosphate buffer saline (PBS, pH 7.4) at 37 °C to mimic physiological conditions. All hydrogels showed a decreased release rate with an increase in dextran molecular weight from 6 to 100 kDa, demonstrating a molecule size-dependent release profile (Figure S6a,b, Supporting Information). For the same molecular weight NIR-dextran, there was a larger barrier to diffusion when released from hydrogels with a lower swelling ratio and delayed degradation rate (G2 and G8), resulting in a slower dextran release than from G4 and G6. The cumulative dextran release profiles from the dense hydrogels G2 and G8 exhibited an initial burst release ($\approx 45\%$ of the initial loading amount) over the first 8 h, followed by a sustained, slower release period of up to 108 h (Figure S6b, Supporting Information). Similarly, hydrogels G4 and G6 continuously released dextran for up to 60 h. The above results demonstrated that our designed photoluminescent hydrogels enabled the loading and sustained release of biotherapeutics, and possible mechanisms of release included diffusion and polymer degradation.

2.5. In Vitro Cytotoxicity Evaluation, Cell Encapsulation, and Scanning Electron Microscopy (SEM) Imaging Studies

XTT assay was performed to determine the effects of the different hydrogels we developed on the viability of NIH-3T3 fibroblasts and MCF-7 cells. Cell viabilities following 2 d culture of NIH-3T3 fibroblasts and MCF-7 cells with extracts from CHPO-Ser-ET/eight-arm PEG hydrogels (G2, G4, G6, and G8) are shown in Figure 5a,b. The results showed that all the cell viabilities were maintained at about 90% and were comparable to cell culture plastic controls, indicating that the degradation products of the designed hydrogels had minimal cytotoxicity. Since the building blocks of the polyester oligomers (which make up the hydrogels) are a nontoxic metabolic product (citric acid), an amino acid (serine or cysteine), and an FDA-approved biomaterial (PEG), the hydrogel products would be most likely biocompatible. Moreover, Michael addition cross-linking avoids the use of cytotoxic molecules and can be carried out under mild physiological conditions.^[13]

Well-designed hydrogel scaffolds generally exhibit good biocompatibility, provide support for donor cells, and possess tunable mechanical properties and chemical structures that allow biofunctionalization to influence biomaterial–host interactions. To promote cell adhesion and proliferation, maleimide groups of eight-arm PEG were partially modified with extracellular matrix (ECM)-derived peptides such as CRGDS, followed by reaction with CHPO-Ser-ET to yield G2 hydrogels incorporated with CRGDS. NIH-3T3 fibroblasts were then seeded onto the peptide-functionalized G2 hydrogels (CRGDS-G2) and cell growth was monitored over time to evaluate hydrogel biocompatibility. As shown in Figure 5c, the CRGDS-G2 hydrogel supported cell attachment and spreading, and the hydrogel surface was covered by cell layers at 48 h. These all improved the cytocompatibility and design flexibility of the hydrogel, and made them promising materials as injectable implants with

photoluminescence for local delivery of therapeutic proteins, compounds, and cells.

Inherent properties of biomaterials such as microstructure and stiffness are significant factors that affect cell–matrix interactions. Previous studies have shown that cells preferred a stiff substrate rather than a soft one for *in vitro* 2D culture, while a softer 3D environment was desirable to facilitate stretch and proliferation of cells when encapsulated.^[14] In this study, SEM measurement was performed to examine the microstructure morphologies of G2 and G6 hydrogels. As shown in Figure 5d,e, G2 hydrogel had a tight and dense structure, indicating a relatively high crosslink density. This was consistent with the above studies that G2 showed strong yield stress and storage modulus than G6 hydrogel, as well as excellent biocompatibility for 2D culture. Compared with G2 hydrogel, a looser, more porous and interconnect appearance was observed for G6 hydrogel which was formulated via crosslinking of thiols and acrylates (Figure 5f,g). A minor change in functional groups of eight-arm PEG was attributed to difference in crosslink density. CRGDS-G6 hydrogel was used for 3D cell culture due to its porous structure and lower yield stress. SEM illustrated that NIH-3T3 cells attached to the hydrogel surface (Figure 5h), migrated and stretched into the porous material (Figure 5i). In this regard, CHPO-Ser-ET/PEG hydrogels could be a promising class of injectable scaffolds with good *in vitro* biocompatibility, and their composition would allow for flexibility of biofunctionalization to further improve material–cell interaction.

2.6. In Vivo Evaluation of Biocompatibility and Bioimaging of Photoluminescent Hydrogels

To test whether the optical property of the photoluminescent hydrogels would allow *in vivo* bioimaging and implant tracking, CHPO-Ser-ET/eight-arm PEG and CHPO-Cys-ET/eight-arm PEG hydrogels were first examined *in vitro* using a gel imaging system (Figure 6). Figure S7a,b (Supporting Information) showed that only CHPO-Ser-ET/PEG hydrogel exhibited photoluminescence when exposed to a wavelength of 488 nm, which was consistent with the above fluorescent excitation spectrum characterization of the two hydrogels (Figure 3f). Thus, the precursor solutions of CHPO-Ser-ET/PEG hydrogels (G2, G4, G6, and G8) were injected beneath the skin of the Balb/c or nude mice as indicated by the arrow (Figure 7a). The mice were then imaged using *in vivo* fluorescent imaging system to track the fluorescence decay of *in situ* formed hydrogel implants. As shown in Figure 7b, the CHPO-Ser-ET/PEG hydrogels were readily detected and visualized under 488 nm excitation and 525 nm emission *in vivo*, which enabled noninvasive monitoring of the injected implants without extracting the implants or sacrificing animals. It is noteworthy that the injected hydrogel underwent degradation via hydrolysis of ester bonds. During degradation process, the random breaking of ester bonds resulted in fluorescence loss, making it possible to track *in vivo* degradation in hydrogel implants by measuring their fluorescent signal decay. As shown in Figure 7c, fluorescence signal of the hydrogel implants was tracked every day after s.c. injection. When compared with G4 and G6, G2 and G8 hydrogels demonstrated slower *in vivo* fluorescence loss

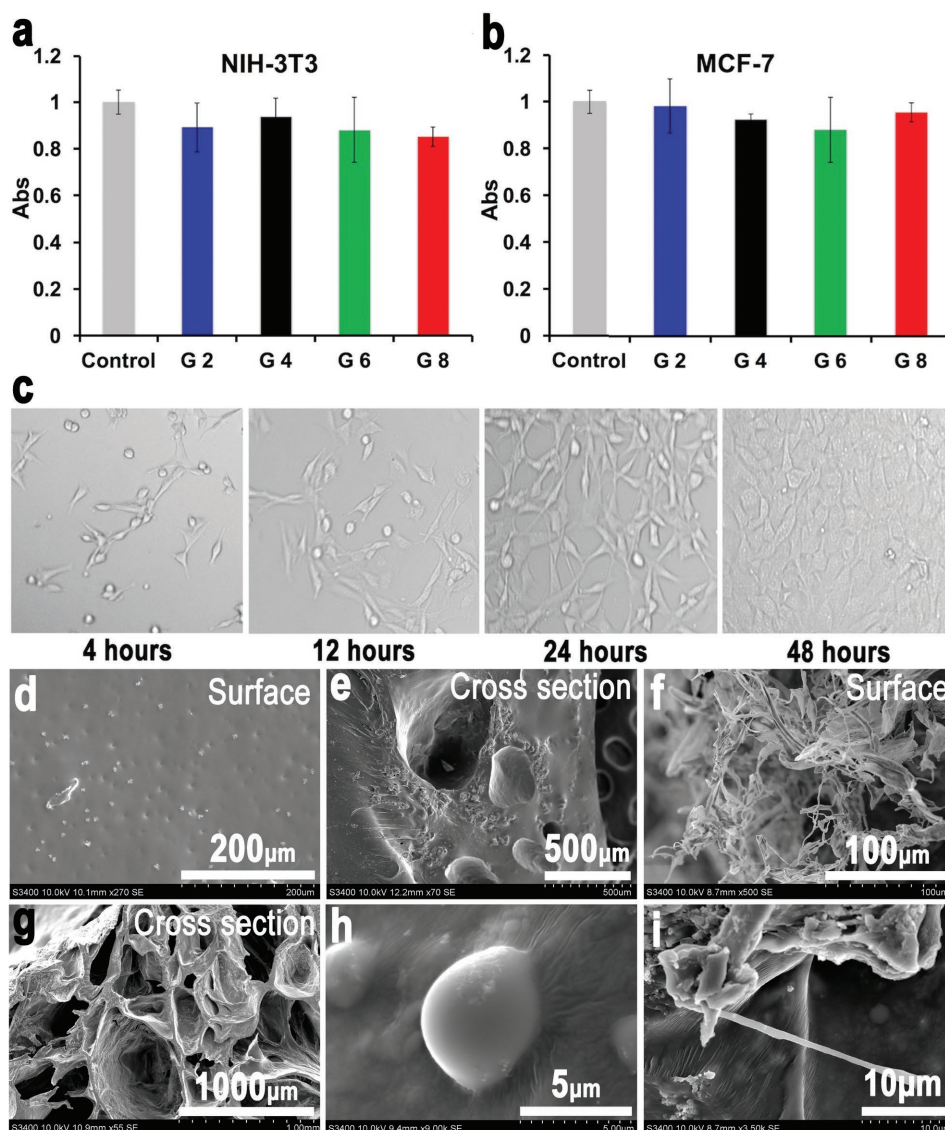


Figure 5. In vitro cell culture studies and cytotoxicity evaluation, and SEM images of photoluminescent hydrogels. a, b) Cell viability assay (XTT assay) for NIH-3T3 and MCF-7 cells cultured with extracts of different CHPO-Ser-ET/eight-arm PEG hydrogel samples. (Cells cultured on the plastic surface of cell culture plates were used as controls. Data were analyzed via Student's *t*-test, which indicated a *P*-value > 0.05 when comparing cell culture plastic controls to the other groups.) Data are presented as the mean ± standard deviation (*n* = 5). c) NIH-3T3 cells attached to and spread on the surface of CRGDS-G2 hydrogel disk over time. SEM images of photoluminescent hydrogel scaffolds d, e) G2 and f, g) G6. h, i) SEM images of CRGDS-G6 hydrogel seeded with NIH-3T3.

rate, indicating that G2 and G8 had a lower in vivo degradation rate. This result matched the trend from their in vitro degradation rates, and was the most likely result of their higher cross-link density and lower porosity. Additionally, weak emission at 725 nm (near-infrared wavelength range) was detected in the subcutaneous CHPO-Ser-ET/PEG hydrogel implants upon excitation at 500 nm (data not shown). No fluorescence was detected in treated mice and gel bumps all disappeared by day 7 following s.c. injection, indicating complete in vivo degradation of the injected hydrogel implants. Correlating in vivo fluorescent signal with hydrogel degradation properties may provide important insights on interactions between injected implants and tissues in situ and in real time.

Hematoxylin and eosin (H&E) staining and immunohistochemical staining was performed to evaluate in vivo biocompatibility of the injectable hydrogel implant. Following s.c. injection of G2 precursor solution, in situ hydrogel formation was observed beneath the skin of Balb/C mice (Figure 8a). The skin tissues were harvested at day 7 post s.c. injection and sectioned for image analysis. H&E staining illustrated that no edema, tissue necrosis, or epithelial erosion was observed during hydrogel degradation process. There was no significant difference between the tissues with and without hydrogel injection (Figure 8b,c). As shown in Figure 8d,e, immunostaining against CD68⁺ macrophages confirmed that the injected hydrogel implants did not induce inflammation, providing

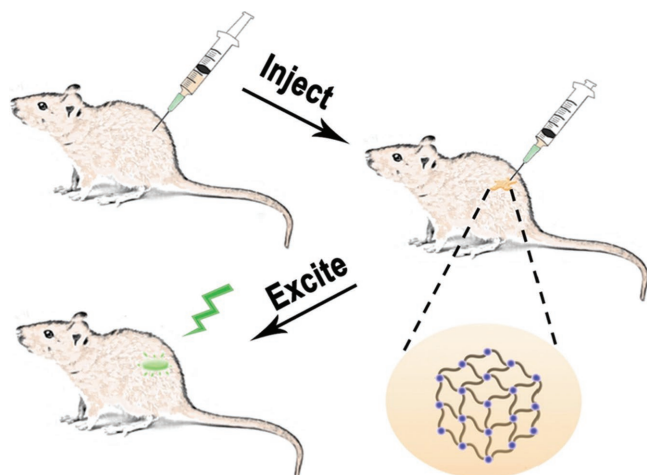


Figure 6. Schematic illustration of in vivo tracking of photoluminescent hydrogel implants.

further evidence of hydrogel biocompatibility. With excellent in vivo biocompatibility and unique intrinsic fluorescence properties, CHPO-Ser-ET/PEG hydrogels could be used as both label-free in vivo imaging tools and injectable scaffolds with drug release capacity.

3. Conclusion

In conclusion, we have successfully synthesized and characterized a library of biodegradable and intrinsically photoluminescent hydrogels. These injectable hydrogels emitted strong and tunable fluorescence, and demonstrated excellent in vitro and in vivo biocompatibility. These materials also exhibited diverse properties including curing time, swelling, degradation, mechanical properties, and release of model polysaccharides, which could be tailored for a variety of biomedical applications by adjusting chemical composition and gelation conditions in hydrogel formulation. Additionally, the photoluminescent hydrogels supported cell growth in vitro, and could serve as injectable scaffolds and be detected in vivo under visible light, enabling noninvasive fluorescence imaging for tracking in vivo degradation of the injected scaffolds. This new class of photoluminescent hydrogels can potentially be used as both label-free in vivo imaging tools and in situ curing injectable scaffolds for a wide variety of applications including tissue regeneration and drug delivery.

4. Experimental Section

Synthesis of Polyester Oligomers CHPO-Ser-ET and CHPO-Cys-ET: For CHPO-Ser (or CHPO-Cys) synthesis, equimolar amounts of citric acid (1.99 g) and hexaethylene glycol (2.13 g) were added to a 100 mL two-neck round bottom flask for ≈ 120 min at 155 °C under nitrogen protection. The mixture was stirred, followed by the addition of serine (or L-cysteine) at a molar ratio of 1:0.2 (citric acid:amino acid) for another 80 min. The oligomers were cooled at room temperature and then purified through a dialysis method (0.5–1 kDa) followed by freeze drying. The yield of CHPO-Ser oligomer was $\approx 82\%$.

CHPO-Ser-ET (or CHPO-Cys-ET) was synthesized through the transesterification of CHPO-Ser (or CHPO-Cys) with ethyl thioglycolate using CALB-immobilized on acrylic resin as the catalyst. Briefly, CHPO-Ser (or CHPO-Cys) was dissolved in acetonitrile, followed by the addition of ethyl thioglycolate and CALB (molar ratio of ethyl thioglycolate to citric acid is 2.2:1). The mixture was stirred at 55–60 °C under nitrogen protection for 7 h. CALB was filtered and the resultant thiol-modified oligomer CHPO-Ser-ET (or CHPO-Cys-ET) was purified through dialysis by using a dialysis tubing (1 kDa). The yield of CHPO-Ser-ET oligomers was $\approx 73\%$.

^1H and ^{13}C nuclear magnetic resonance (NMR) spectra were recorded on a Bruker 500 MHz NMR spectrometer. FTIR spectra were collected using a Nicolet IS-10 (Thermo Fisher Scientific). Molecular weight of the yielded polyester oligomers was characterized using MALDI-TOF-MS (Bruker).

Hydrogel Fabrication and Synthesis of CRGDS-Functionalized Eight-Arm PEG Derivatives: Multiarm (four- or eight-arm) PEG derivatives with maleimide or acrylate groups at each arm terminal (molecular weight: 10 000 Da) were used as cross-linking agents. Hydrogels were formulated with multiarm PEG derivatives and photoluminescent CHPO-Ser-ET (or CHPO-Cys-ET) by employing thiol–Michael addition chemistry according to a similar procedure as described in detail previously.^[15] Briefly, CHPO-Ser-ET (or CHPO-Cys-ET) oligomer and multiarm PEG derivatives were dissolved individually in PBS to obtain precursor solutions with predetermined weight concentrations. By mixing the two solutions, hydrogels could be formed in situ within seconds to hours, depending on formulation compositions and gelation conditions.

CRGDS-functionalized eight-arm PEG derivatives were used to formulate peptide-functionalized hydrogels for in vitro cell culture studies. First, eight-arm PEG derivatives and CRGDS peptide were combined with the molar ratio of PEG to peptide to be 1:1, and dissolved in PBS with triethanolamine (TEA).^[16] The mixture was stirred under nitrogen protection to obtain CRGDS-functionalized eight-arm PEG derivatives via a thiol–maleimide or thiol–ene coupling reaction. After being purified by dialysis in water, the solution was lyophilized to yield a white powder product.

Quantum Yield Measurement: The comparative method of Williams was performed to measure the quantum yield of the polyester oligomers (CHPO-Ser-ET and CHPO-Cys-ET).^[17] Briefly, 10% polyester oligomer solutions were prepared. The oligomers solution was scanned at various excitation wavelengths and the optimal excitation wavelength was determined as the one which generated the highest emission intensity. Then, the absorbance = 0, 0.02, 0.04, 0.06, 0.08, and 0.1 at the optimal excitation wavelength of both standards and tested samples were measured for fluorescence intensity (the area of the fluorescence spectrum). A graph of absorbance versus integrated fluorescence intensity was plotted. The fluorescence quantum yields of the polyester oligomers were calculated according to the equation below

$$\phi_x = \phi_{ST} \left(\frac{\text{Grad}_x / \text{Grad}_{ST}}{\eta_x^2 / \eta_{ST}^2} \right) \quad (1)$$

where Φ is the fluorescence quantum yield, Grad is the gradient obtained from the plot of integrated fluorescence intensity versus absorbance, and η is the refractive index of the solvent. x and ST denote tested sample and standard, respectively. Quinine sulfate (in 0.1 M H_2SO_4) or anthracene (in ethanol) was used as standard, depending on their optimal excitation wavelength range. The polyester oligomers were dissolved in water. Absorbance and fluorescence were measured using TECAN Infinite M200 PRO microplate reader.

In Vitro Degradation of Hydrogel: Hydrogel disk samples (≈ 50 μL , diameter = 5.6 mm, height = 2.9 mm) at 10 wt% total oligomers were cured in silicone molds. After lyophilization, dried hydrogel disks were immersed into individual wells of a 48-well plate containing PBS (pH = 7.4) at 37 °C for degradation studies. The initial weight of hydrogels was recorded as W_0 . PBS was changed daily to maintain the pH of the solution at 7.4. At predetermined time points, hydrogel samples were removed from incubation, washed and lyophilized. The weight of dried hydrogels was recorded as W_t . Hydrogel weight loss was

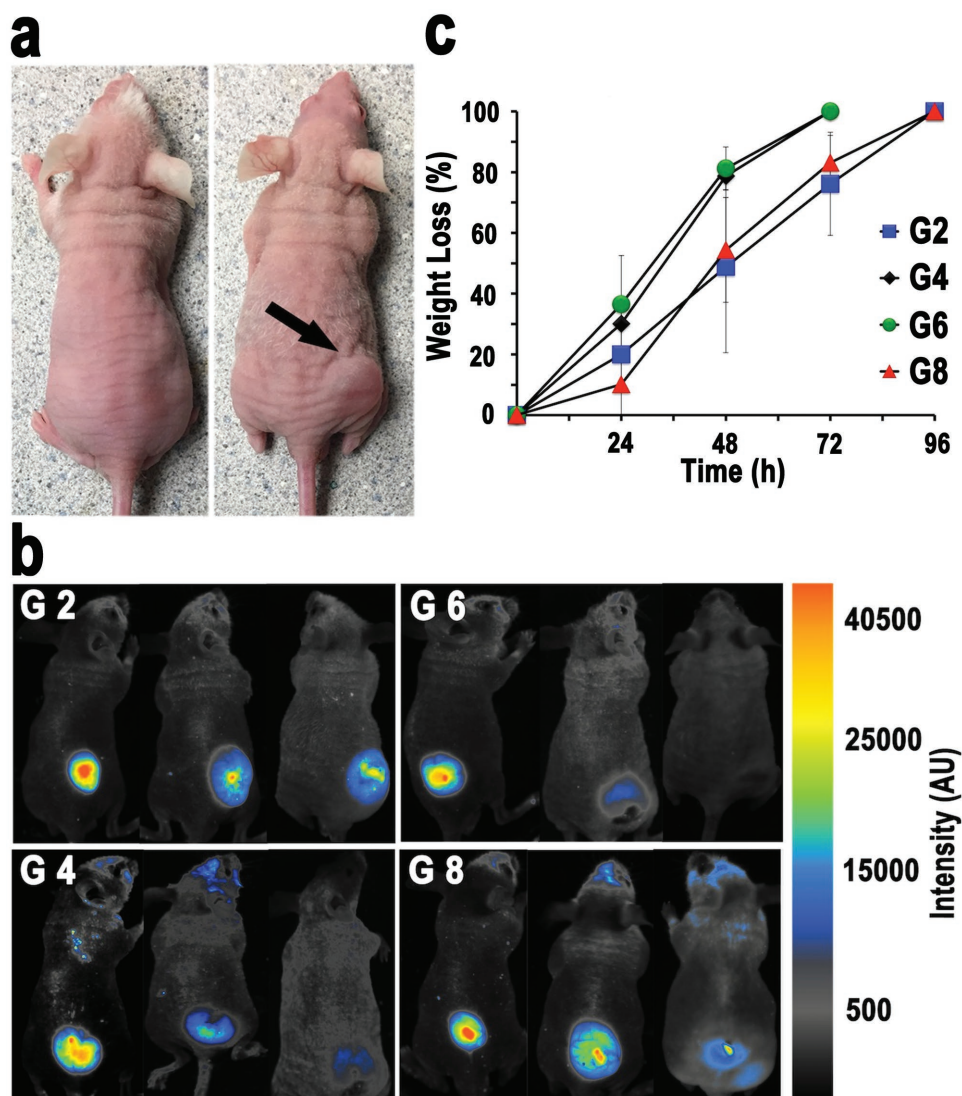


Figure 7. In vivo fluorescence imaging studies. a) Nude mice before and after subcutaneous injection of CHPO-Ser-ET/eight-arm PEG hydrogels (black arrow indicates the site where the hydrogel precursor solution was injected and crosslinked in situ). b) Fluorescence images of nude mice on day 1, 2, and 3 (left to right) following subcutaneous injection of CHPO-Ser-ET/eight-arm PEG-maleimide hydrogels (exposure time: 3 s). c) In vivo degradation profiles of CHPO-Ser-ET/eight-arm PEG hydrogels were depicted by tracking the loss of fluorescence intensity with time following injection, which was converted to weight loss. Data are presented as the mean \pm standard deviation ($n = 5$).

evaluated by comparing the initial weight (W_0) with the weight measured at defined time points as below

$$\text{Mass loss(\%)} = \left[\frac{W_0 - W_t}{W_0} \right] \times 100\% \quad (2)$$

Dynamic Rheology: A Discovery Hybrid Rheometer 3 (DHR-3, TA Instruments, New Castle, DE) was used to characterize hydrogel gelation kinetics and mechanical properties. For each test, hydrogel precursors were sufficiently mixed and a volume of 280 μL was applied to a temperature-controlled stage at preset temperature (25 and 37 $^{\circ}\text{C}$), followed by lowering the 25 mm parallel stainless steel plate to a predetermined gap to initiate the measurement. Dynamic time sweep measurements were made within the linear viscoelastic region (strain = 5%, angular frequency = 1 rad s^{-1}). The storage modulus (G') and loss modulus (G'') were recorded as a function of time. The time point where $\tan(\delta) = 1$ (i.e., G'/G'' cross over) was used to define the gelation time. The time spent between initial hydrogel mixing and

commencement of rheology data collection was ≈ 15 s and was added onto the final gelation time values.

In Vitro Swelling of Measurements: For the swelling rest, cured hydrogel disk samples ($\approx 50 \mu\text{L}$, diameter = 5.6 mm, height = 2.9 mm) were incubated in PBS at 37 $^{\circ}\text{C}$ for 24 h to leach out the unreacted sol fraction. The initial dry hydrogel weight (W_0) was measured after freeze-drying. Samples were then immersed in PBS at 37 $^{\circ}\text{C}$, and allowed to equilibrate for a minimum of 6 h. The swollen hydrogels were accurately weighed (W_t) after gently removing the excess water by the filter paper. The swelling ratio (Q_m) was evaluated by comparing the wet weight with the dry weight of the hydrogel sample

$$Q_m = \left(\frac{W_t}{W_0} \right) \times 100\% \quad (3)$$

NIR-Dextran Release Experiments: NIR-labeled dextrans of two different molecular weights (6 and 100 kDa) were individually encapsulated in CHPO-Ser-ET/eight-arm PEG hydrogel formulations at a concentration of 500 $\mu\text{g mL}^{-1}$. Hydrogels ($n = 5$ per group) were incubated in 1 mL

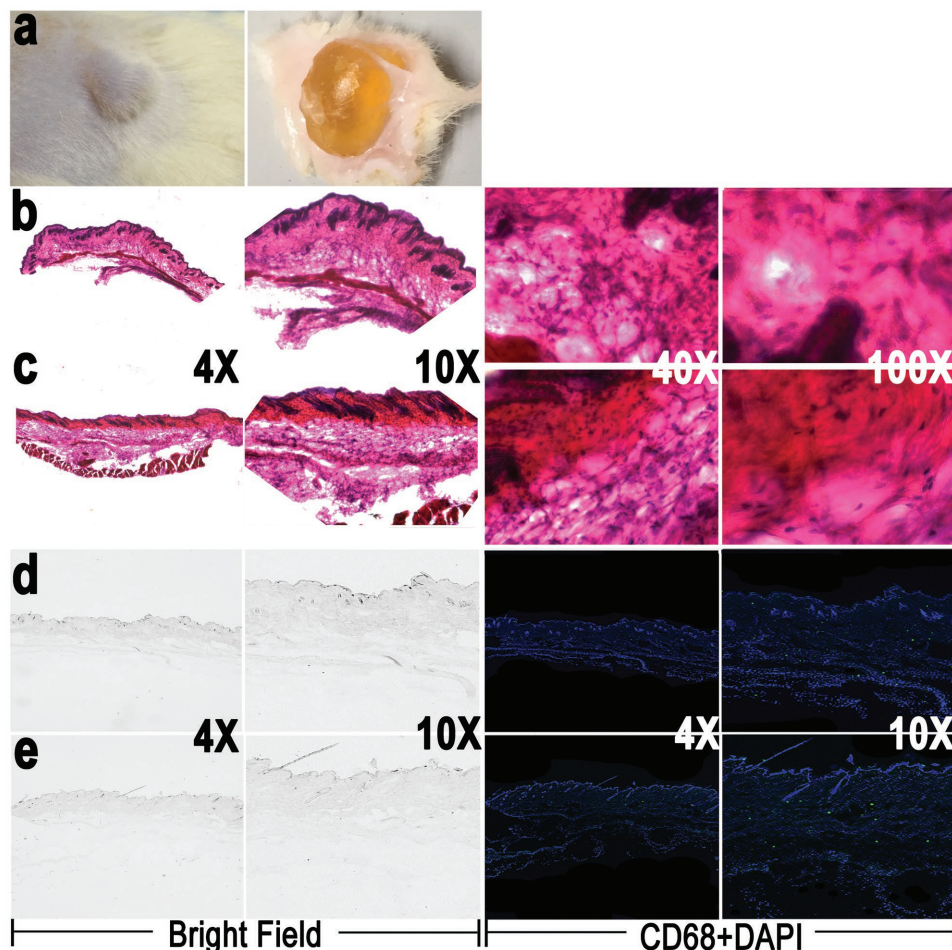


Figure 8. In vivo biocompatibility studies. a) Precursor solutions of G2 hydrogel were subcutaneously injected into the Balb/c mouse, and in situ formation of the hydrogel was observed beneath the skin. The tissue at injection site was then harvested and sectioned for imaging analysis. b) Representative images of H&E stained tissue sections from injected mice (magnifications 4x, 10x, 40x, and 100x). c) Representative images of H&E stained tissue sections harvested from untreated mice at the same site as injected mice (control group, magnifications 4x, 10x, 40x, and 100x). d,e) Representative images of immunostained tissue sections with and without G2 hydrogel injection (magnifications 4x and 10x. Left two images: bright field. Right two images: merged from Figure S8a,b (Supporting Information)). Cell nuclei stained blue (DAPI), and macrophages stained green (anti-CD68). Images are representative of $n = 5$.

of PBS (changed daily) at 37 °C. Duplicate 200 μL aliquots of the incubation media for each sample were analyzed at defined time points for fluorescent intensity (ex/em 754/783) on an Infinite M200 PRO microplate reader (TECAN).

Cell Culture and In Vitro Studies: Hydrogel disk samples ($\approx 50 \mu\text{L}$, diameter = 5.6 mm, height = 2.9 mm) were fabricated and sterilized by 70% ethanol and UV light prior to use. Each hydrogel sample was then incubated in 1 mL of Dulbecco's modified Eagle's medium (DMEM) for 72 h at 37 °C. After being sterilized by filtration (0.22 μm), the hydrogel extract was supplemented with 10% fetal bovine serum (FBS). NIH-3T3 and MCF-7 cells were seeded in 96-well culture plate at a density of 5.5×10^4 cells per well and incubated in high glucose DMEM containing 10% FBS, 100 units mL^{-1} penicillin, and 100 $\mu\text{g mL}^{-1}$ streptomycin at 37 °C with 5% CO_2 under fully humidified conditions for 24 h. Then the culture media was replaced with the hydrogel extract. After another 48 h of incubation, XTT assay was performed according to the manufacturer's instructions to examine cell viability and proliferation. Cells cultured on the plastic surface of cell culture plates were used as controls.

CRGDS-functionalized hydrogels CRGDS-G2 were casted in Corning ultralow attachment 96-well plates (Fisher Scientific, Pittsburgh, PA) and sterilized by 70% ethanol and UV light. NIH-3T3 cells ($10\,000 \text{ cells cm}^{-2}$)

were seeded onto each CRGDS-G2 hydrogel, and allowed to incubate at 37 °C with 5% CO_2 to allow cell attachment. The culture medium was replaced every day. At defined time points, cell morphology was observed and imaged using microscope (Keyence, Itasca, IL).

Cell growth within CRGDS-G6 hydrogel was imaged by SEM. Sterilized thiolated polyester oligomer CHPO-Ser-ET was added to 20 μL volume of a suspension of NIH-3T3 cells (2×10^5 cells). The resultant suspension was then mixed with sterilized CRGDS-functionalized eight-arm PEG-acrylate solution to form cell-containing CRGDS-G6 hydrogels as described above. Each hydrogel sample was incubated in supplemented DMEM (changed daily) at 37 °C with 5% CO_2 . After 2 d incubation, samples were first placed into PBS for 10 min (three times) and fixed with 4% glutaraldehyde in PBS for 1 h at room temperature followed by washing three times with water. The fixed samples were freeze-dried and sputter-coated with gold. The morphology of cells on the surface or cross section of hydrogel scaffold was observed via SEM.

In Vivo Bioimaging and Biocompatibility Evaluation: Balb/c wild type and nude mice were purchased from Jackson Laboratory. Animals were cared for in compliance with the regulations of the Institutional Animal Care and Use Committee (IACUC) of the Rutgers University (Newark, NJ). All animal studies were approved by the IACUC, Rutgers University.

Before in vivo imaging studies, different hydrogel formulations were first examined in vitro using a PXi gel imaging system (Syngene, Frederick, MD), which demonstrated that the optical property of CHPO-Ser-ET/eight-arm PEG hydrogels would allow in vivo bioimaging and implant tracking.

Following s.c. injection of sterilized well-mixed precursor solutions (100 μ L, for CHPO-Ser-ET/eight-arm PEG hydrogels), each hydrogel was cured in situ in mice subcutaneous pockets ($n = 5$ for each formulation group). The mice were then imaged daily with excitation wavelength of 488 nm and emission wavelength of 525 nm using an IVIV Spectrum bioluminescent and fluorescent imaging system (Caliper Life Sciences) for 7 d postinjection. The fluorescence intensity was analyzed using Living Image (Caliper Life Sciences, Inc.) acquisition and analysis software.

The mice were sacrificed at day 7 postinjection and skin tissue samples surrounding the hydrogel implants were harvested, frozen with optimum cutting temperature (OCT) compound (Tissue-Tek, Sakura Finetek USA Inc.), and sectioned (10 μ m thick) using a Leica CM3050 S cryostat for H&E staining to preliminarily evaluate in vivo host responses to the hydrogel implants.

Tissue samples were also examined for signs of inflammation (macrophage marker CD68) using immunohistochemical staining. Tissue sections were fixed with precooled acetone and methanol (1:1, vol/vol), and blocked with bovine serum albumin in 0.25% Triton X-100 in PBS. Primary antibody (Anti-CD68, 1:100, Abcam, Cambridge, MA) was applied overnight at 4 $^{\circ}$ C. Secondary antibody (1:250, Life Technologies, Carlsbad, CA) was added after the primary antibody was removed and rinsed with PBS for three times. Tissue sections were counterstained with Prolong Gold Antifade Reagent with DAPI (Life Technologies, Carlsbad, CA). Fluorescent images were colored to show positive nucleus staining in blue and positive staining of microphage in green. The skin tissue harvested from untreated mice at the same site as injected mice were stained and imaged as a control.

Each experiment was performed at least three times. Data were analyzed via Student's *t*-test and presented as mean \pm standard deviation. A *P*-value ≤ 0.05 was considered to denote statistical significance.

Supporting Information

Supporting Information is available from the Wiley Online Library or from the author.

Acknowledgements

Y.-H. Tsou and X.-Q. Zhang contributed equally to this work. The financial support coming from New Jersey Institute of Technology (NJIT) startup funding, New Jersey Health Foundation (PC102-17), and NSF Innovation Corps (1723667) program is gratefully acknowledged. X.-Q. Zhang acknowledges the support from Thousand Talents Plan for Young Professionals.

Conflict of Interest

The authors declare no conflict of interest.

Keywords

biodegradable hydrogels, injectable hydrogels, photoluminescent hydrogels

Received: April 16, 2018

Revised: June 2, 2018

Published online:

- [1] G. Perale, F. Rossi, E. Sundstrom, S. Bacchiega, M. Masi, G. Forloni, P. Veglianese, *ACS Chem. Neurosci.* **2011**, *2*, 336.
- [2] a) D. Seliktar, *Science* **2012**, *336*, 1124; b) Y. Wang, G. A. Ameer, B. J. Sheppard, R. Langer, *Nat. Biotechnol.* **2002**, *20*, 602; c) L. L. Lock, Y. Li, X. Mao, H. Chen, V. Staedtke, R. Bai, W. Ma, R. Lin, Y. Li, G. Liu, *ACS Nano* **2017**, *11*, 797.
- [3] Y.-H. Tsou, J. Khoneisser, P.-C. Huang, X. Xu, *Bioact. Mater.* **2016**, *1*, 39.
- [4] a) C. Wang, R. R. Varshney, D. A. Wang, *Adv. Drug Delivery Rev.* **2010**, *62*, 699; b) B. M. Watson, T. N. Vo, A. M. Tatar, S. R. Shah, D. W. Scott, P. S. Engel, A. G. Mikos, *Biomaterials* **2015**, *67*, 286; c) Y. Li, J. Rodrigues, H. Tomas, *Chem. Soc. Rev.* **2012**, *41*, 2193; d) J. D. Kretlow, S. Young, L. Klouda, M. Wong, A. G. Mikos, *Adv. Mater.* **2009**, *21*, 3368; e) J. Li, X. Li, X. Ni, X. Wang, H. Li, K. W. Leong, *Biomaterials* **2006**, *27*, 4132; f) E. R. Ruskowitz, C. A. DeForest, *Nat. Rev. Mater.* **2018**, *3*, 17087.
- [5] a) N. Artzi, N. Oliva, C. Puron, S. Shitreet, S. Artzi, A. bon Ramos, A. Groothuis, G. Sahagian, E. R. Edelman, *Nat. Mater.* **2011**, *10*, 704; b) S. H. Kim, J. H. Lee, H. Hyun, Y. Ashitate, G. Park, K. Robichaud, E. Lunsford, S. J. Lee, G. Khang, H. S. Choi, *Sci. Rep.* **2013**, *3*, 1198; c) V. Yesilyurt, M. J. Webber, E. A. Appel, C. Godwin, R. Langer, D. G. Anderson, *Adv. Mater.* **2016**, *28*, 86.
- [6] a) J. Li, X. Hong, Y. Liu, D. Li, Y. W. Wang, J. H. Li, Y. B. Bai, T. J. Li, *Adv. Mater.* **2005**, *17*, 163; b) A. Berdichevski, H. S. Yameen, H. Dafni, M. Neeman, D. Seliktar, *Proc. Natl. Acad. Sci. USA* **2015**, *112*, 5147; c) A. M. Breul, M. D. Hager, U. S. Schubert, *Chem. Soc. Rev.* **2013**, *42*, 5366; d) M. X. Wang, C. H. Yang, Z. Q. Liu, J. Zhou, F. Xu, Z. Suo, J. H. Yang, Y. M. Chen, *Macromol. Rapid Commun.* **2015**, *36*, 465; e) J. C. Bunzli, C. Piguet, *Chem. Soc. Rev.* **2005**, *34*, 1048.
- [7] Z. Wang, Y. Zhang, J. Zhang, L. Huang, J. Liu, Y. Li, G. Zhang, S. C. Kundu, L. Wang, *Sci. Rep.* **2014**, *4*, 7064.
- [8] a) J. K. Jaiswal, H. Mattoussi, J. M. Mauro, S. M. Simon, *Nat. Biotechnol.* **2003**, *21*, 47; b) Y. Zhang, R. T. Tran, I. S. Qattan, Y. T. Tsai, L. Tang, C. Liu, J. Yang, *Biomaterials* **2013**, *34*, 4048.
- [9] R. Hardman, *Environ. Health Perspect.* **2006**, *114*, 165.
- [10] C. P. Montgomery, B. S. Murray, E. J. New, R. Pal, D. Parker, *Acc. Chem. Res.* **2009**, *42*, 925.
- [11] a) J. Yang, Y. Zhang, S. Gautam, L. Liu, J. Dey, W. Chen, R. P. Mason, C. A. Serrano, K. A. Schug, L. Tang, *Proc. Natl. Acad. Sci. USA* **2009**, *106*, 10086; b) Z. Xie, Y. Zhang, L. Liu, H. Weng, R. P. Mason, L. Tang, K. T. Nguyen, J. T. Hsieh, J. Yang, *Adv. Mater.* **2014**, *26*, 4491; c) D. Gyawali, S. Zhou, R. T. Tran, Y. Zhang, C. Liu, X. Bai, J. Yang, *Adv. Healthcare Mater.* **2014**, *3*, 182.
- [12] T. M. O'Shea, A. A. Aimettil, E. Kim, V. Yesilyurt, R. Langer, *Adv. Mater.* **2015**, *27*, 65.
- [13] Y. Zhou, W. Nie, J. Zhao, X. Yuan, *J. Mater. Sci.: Mater. Med.* **2013**, *24*, 2277.
- [14] a) D. E. Discher, P. Janmey, Y. L. Wang, *Science* **2005**, *310*, 1139; b) W. L. Murphy, T. C. McDevitt, A. J. Engler, *Nat. Mater.* **2014**, *13*, 547; c) J. Thiele, Y. Ma, S. M. Bruekers, S. Ma, W. T. Huck, *Adv. Mater.* **2014**, *26*, 125.
- [15] C. D. Pritchard, T. M. O'Shea, D. J. Siegwart, E. Calo, D. G. Anderson, F. M. Reynolds, J. A. Thomas, J. R. Slotkin, E. J. Woodard, R. Langer, *Biomaterials* **2011**, *32*, 587.
- [16] E. A. Phelps, N. O. Enemchukwu, V. F. Fiore, J. C. Sy, N. Murthy, T. A. Sulchek, T. H. Barker, A. J. Garcia, *Adv. Mater.* **2012**, *24*, 64.
- [17] A. T. R. Williams, A. Stephen, J. N. Miller, *Analyst* **1983**, *24*, 1067.